

# BN-Enabled Epitaxy of $\text{Pb}_{1-x}\text{Sn}_x\text{Se}$ Nanoplates on $\text{SiO}_2/\text{Si}$ for High-Performance Mid-Infrared Detection

Qisheng Wang, Yao Wen, Fengrui Yao, Yun Huang, Zhenxing Wang, Molin Li, Xueying Zhan, Kai Xu, Fengmei Wang, Feng Wang, Jie Li, Kaihui Liu, Chao Jiang, Fengqi Liu,\* and Jun He\*

Surface electronic properties of supporting substrates are of crucial importance for both crystal growth and devices performance due to the fact that this surface (1) governs the initial nucleation<sup>[1]</sup> and interface lattice orientation<sup>[2]</sup> during the growth of crystals, and (2) strongly affects the charge-carrier transport<sup>[3,4]</sup> of field-induced transistor and optoelectronic devices. However, typical functional substrates such as silicon dioxide/silicon ( $\text{SiO}_2/\text{Si}$ ), glass, and plastic are amorphous with high degree of disorders, which impedes, on the one hand, the direct epitaxial growth of low-dimensional single crystalline semiconductors on them with long-range order interface and, on the other hand, severely degrades the quality of electronic and optoelectronic devices owing to increasing carrier scattering or localization caused by surface defect states.<sup>[5]</sup> Although the synthesized nanomaterials can be transferred from growth wafer to these functional substrates such as  $\text{SiO}_2/\text{Si}$ , by complicated chemical approach,<sup>[6,7]</sup> it inevitably damages or contaminates the target products due to the utilization of corrosive acid or organic solvent.

Recent development in both synthesis and device of 2D layered materials<sup>[8–10]</sup> inspires us that van der Waals epitaxy (vdWE) could be a new route for solving the above problem. This concept, with the utilization of layered materials whose

surfaces are free of dangling bonds, allows the direct growth of a highly lattice-mismatched system.<sup>[11]</sup> Meanwhile, epilayer is perfectly relaxed without excessive strain in the heterointerface since overlayer interacts with substrate through weak van der Waals (vdW) force. vdWE has been successfully used to grow single-crystalline organic molecules on graphene or boron nitride (BN).<sup>[12]</sup> Intriguingly, vdW substrates can significantly improve the electronic performance of epilayer since their surfaces are free of dangling bonds with low density of surface defect states.<sup>[3,13]</sup> All above features imply, by utilizing vdW substrates as the thermal/lattice mismatch buffer layer, high-quality single-crystalline 2D semiconductors beyond layered materials can be directly grown on  $\text{SiO}_2/\text{Si}$  substrates. And considerable progress in large-scale synthesis and clean transfer of 2D layered materials lay a foundation for us to realize this design,<sup>[7,14,15]</sup> which will not only improve their electronic performance but also promote their practical applications in current semiconductor industry due to the highly compatible of  $\text{SiO}_2/\text{Si}$  substrates with the existing Si-based integration circuit technologies.

$\text{Pb}_{1-x}\text{Sn}_x\text{Se}$  is a direct narrow band gap semiconductor with great application potential in infrared detection and thermoelectric conversion.<sup>[16]</sup> Bulk  $\text{Pb}_{1-x}\text{Sn}_x\text{Se}$  exhibits highly efficient photodetection in the range of 3–5  $\mu\text{m}$  which is matched with mid-infrared atmosphere window, an important communication waveband. Significantly,  $\text{Pb}_{1-x}\text{Sn}_x\text{Se}$  is recently discovered to be one of the topological crystalline insulators with robust surface states residing on high-symmetry surfaces.<sup>[17]</sup> And its surface state can be manipulated by strain or electrical field, which suggests high-speed logic devices could be developed based on  $\text{Pb}_{1-x}\text{Sn}_x\text{Se}$ . It is worth noting that 2D  $\text{Pb}_{1-x}\text{Sn}_x\text{Se}$  nanostructures (1) profoundly enhance topological states due to their dominant top and bottom surface and (2) make the electrostatic field modulation more efficient due to ultrathin thickness in the vertical direction. Recently, we have developed a general strategy for controlled growth of ultrathin  $\text{Pb}_{1-x}\text{Sn}_x\text{Se}$  nanoplates on layered mica by vdWE.<sup>[18,19]</sup> However, on the one hand, the flexible mica substrate is incompatible with modern functional devices fabrication technology and, on the other hand, it is extremely difficult to transfer  $\text{Pb}_{1-x}\text{Sn}_x\text{Se}$  nanoplates from mica to functional substrates like  $\text{SiO}_2/\text{Si}$  without contaminating or destroying the samples. As a result, it is meaningful to develop a controllable synthesis method of 2D  $\text{Pb}_{1-x}\text{Sn}_x\text{Se}$

Q. Wang, Y. Wen, Y. Huang, Prof. Z. Wang, M. Li, X. Zhan, K. Xu, F. M. Wang, F. Wang, J. Li, Prof. C. Jiang, Prof. J. He  
CAS Key Laboratory of Nanosystem and Hierarchical Fabrication  
National Center for Nanoscience and Technology  
Beijing 100190, P. R. China  
E-mail: hej@nanoctr.cn

F. Yao, Prof. K. Liu  
School of Physics  
Peking University  
Beijing 100871, P. R. China  
Prof. F. Liu  
Key Laboratory of Semiconductor Materials Science  
Institute of Semiconductor  
Chinese Academy of Science  
Beijing 100083, P. R. China  
E-mail: fqliu@red.semi.ac.cn



DOI: 10.1002/sml.201502049

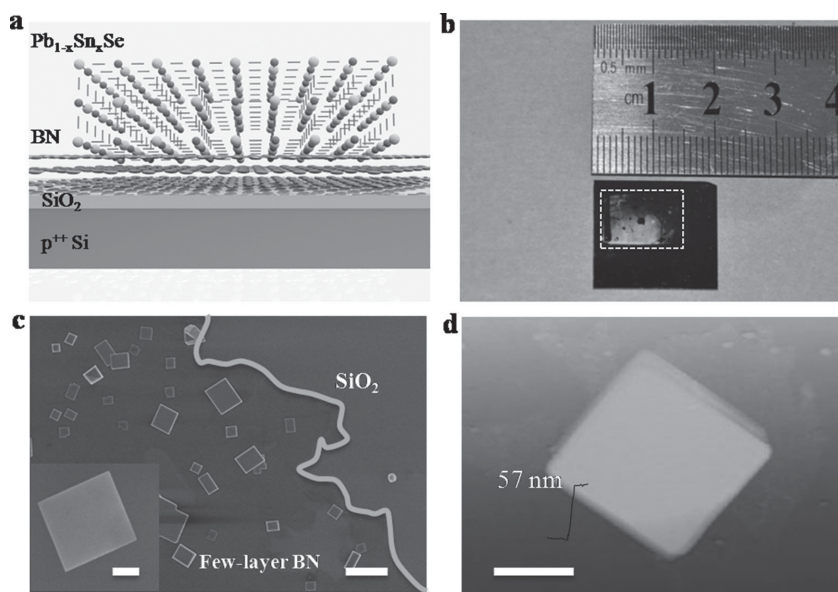


**Figure 1.** Few-layer BN-enabled epitaxy of  $\text{Pb}_{1-x}\text{Sn}_x\text{Se}$  nanoplates on  $\text{SiO}_2/\text{Si}$ . a) Schematic illustration for epitaxial growth of  $\text{Pb}_{1-x}\text{Sn}_x\text{Se}$  nanoplates on  $\text{SiO}_2/\text{Si}$  by designing a buffer layer of few-layer BN. b) Photograph of  $\text{Pb}_{1-x}\text{Sn}_x\text{Se}$  nanoplates on few-layer BN-covered  $\text{SiO}_2/\text{Si}$  substrate. The white and dashed square labels the region that was covered by few-layer BN. c)  $\text{Pb}_{1-x}\text{Sn}_x\text{Se}$  nanoplates only grow on this region which can be further observed by SEM image. The inset in (c) is an amplified SEM image of one  $\text{Pb}_{1-x}\text{Sn}_x\text{Se}$  nanoplate. d) AFM image of one typical  $\text{Pb}_{1-x}\text{Sn}_x\text{Se}$  nanoplate on few-layer BN. The scale bar in inset of (c) and (d) are 200 nm, 3  $\mu\text{m}$ , and 2  $\mu\text{m}$ , respectively.

on  $\text{SiO}_2/\text{Si}$  for exploiting high-performance and Si-compatible electronic devices.

Here, we report an epitaxial growth of highly single-crystalline 2D  $\text{Pb}_{1-x}\text{Sn}_x\text{Se}$  nanoplates on amorphous  $\text{SiO}_2/\text{Si}$  by the introduction of a few-layer BN buffer layer. We show few-layer BN plays a vital role for the growth of single-crystalline  $\text{Pb}_{1-x}\text{Sn}_x\text{Se}$  nanoplates since it provides a chemically inert surface for vdWE that effectively screens the chemical bonding interaction generated by disorders on surface of amorphous  $\text{SiO}_2$ . Benefiting high compatibility of  $\text{SiO}_2/\text{Si}$  substrates with current microfabrication industry, we in situ constructed functional devices of  $\text{Pb}_{1-x}\text{Sn}_x\text{Se}$  nanoplates, showing high room-temperature field effect mobility (0.73–4.90  $\text{cm}^2 \text{V}^{-1} \text{s}^{-1}$ ) which is comparable to those of layered materials and molecular crystals, and efficient mid-infrared detection (1.9–2.0  $\mu\text{m}$ ) with photoresponsivity of 318  $\text{mA W}^{-1}$ .

The schematic diagram of our design for epitaxial growth of  $\text{Pb}_{1-x}\text{Sn}_x\text{Se}$  nanoplates on a  $\text{SiO}_2/\text{Si}$  substrate is presented in **Figure 1a**. For the purpose of eliminating the electronic interaction from charged impurities or defects on the surface of amorphous  $\text{SiO}_2$ , few-layer BN was synthesized and then transferred to  $\text{SiO}_2/\text{Si}$ . The synthesis and transfer of few-layer BN have been widely studied in other works<sup>[7,14,20]</sup> (see more in the Experimental Section). Atomic force microscopy (AFM) image of one representative few-layer BN is shown in Figure S1 (Supporting Information). This few-layer BN displays thickness of 1.98 nm with root mean square roughness of 0.329 nm. Some wrinkles, important for the nucleation of  $\text{Pb}_{1-x}\text{Sn}_x\text{Se}$  nanoplates, are also observed on the surface of few-layer BN. And then  $\text{Pb}_{1-x}\text{Sn}_x\text{Se}$  nanoplates are

synthesized by chemical vapor deposition (CVD) on few-layer BN-covered  $\text{SiO}_2/\text{Si}$  substrates. Source and substrate temperatures are set to 600 and 460  $^\circ\text{C}$ , respectively. More experimental details about CVD growth of  $\text{Pb}_{1-x}\text{Sn}_x\text{Se}$  nanoplates are described in our previous work<sup>[19]</sup> and the Experimental Section. Figure 1b and Figure S2 (Supporting Information) show the photographs of typical samples from which we can see  $\text{Pb}_{1-x}\text{Sn}_x\text{Se}$  nanoplates selectively grow on the regions covered by few-layer BN. This feature can be further confirmed by the scanning electron microscopy (SEM) image of Figure 1c. SEM energy-dispersive X-ray (SEM-EDX) elemental analysis denotes the nanoplates are composed of Pb, Sn, and Se with Sn content ( $x$ ) of about 0.6. The height of  $\text{Pb}_{1-x}\text{Sn}_x\text{Se}$  nanoplates distributes between 15 and 70 nm as shown in Figure 1d and Figures S3 and S4 (Supporting Information), which is consistent with the results reported in our previous work. According to the SEM images in Figure 1c, the average lateral dimension of  $\text{Pb}_{1-x}\text{Sn}_x\text{Se}$  nanoplates is 1.5  $\mu\text{m}$  with uncertainty of 0.2  $\mu\text{m}$ .

The heterostructures of few-layer BN/ $\text{Pb}_{1-x}\text{Sn}_x\text{Se}$  nanoplates are further characterized by Raman and transmission electron microscopy (TEM). **Figure 2a** is the optical microscopy images of  $\text{Pb}_{1-x}\text{Sn}_x\text{Se}$  nanoplates on few-layer BN. Two Raman spectra in Figure 2b are collected from locations 1 and 2, respectively, as signed in Figure 2a. One dominant peak at 1369  $\text{cm}^{-1}$  can be assigned to the  $E_{2g}$  vibration mode of few-layer hexagonal BN.<sup>[8]</sup> And Raman peaks at 99 and 119  $\text{cm}^{-1}$  of  $\text{Pb}_{1-x}\text{Sn}_x\text{Se}$  nanoplates would be due to the vibration of both transverse-optical and longitudinal-optical phonons.<sup>[21]</sup> Raman intensity mappings at 99  $\text{cm}^{-1}$  of  $\text{Pb}_{1-x}\text{Sn}_x\text{Se}$  nanoplates and 1369  $\text{cm}^{-1}$  of  $h$ -BN are performed on the region which is labeled by yellow dashed square as shown in Figure 2a. The uniform distribution of Raman intensity at 99  $\text{cm}^{-1}$  demonstrates  $\text{Pb}_{1-x}\text{Sn}_x\text{Se}$  nanoplate is homogeneous. Raman intensity mapping at peak 1369  $\text{cm}^{-1}$  of BN shows dark contrast in the middle region, this can be ascribed to that this region is covered by  $\text{Pb}_{1-x}\text{Sn}_x\text{Se}$  nanoplate. Figure 2e exhibits the cross-section TEM of one  $\text{SiO}_2/\text{few-layer BN}/\text{Pb}_{1-x}\text{Sn}_x\text{Se}$  nanoplate heterostructure. Details of samples preparation for cross-section TEM are described in the Supporting Information. A sharp interface without apparent lattice distortion between few-layer BN and  $\text{Pb}_{1-x}\text{Sn}_x\text{Se}$  nanoplate can be clearly identified from the high-resolution cross-section TEM (Figure 2f). The lattice space of layered BN (0002) crystal plane is 0.33 nm which is larger than that of  $\text{Pb}_{1-x}\text{Sn}_x\text{Se}$  (020) surface. Thus the lattice mismatch in the interface of  $\text{Pb}_{1-x}\text{Sn}_x\text{Se}/\text{BN}$  reaches 6.1%. This is in good agreement with the characteristic of vdWE which allows the growth of a highly lattice-mismatched system due to weak vdW interaction in the interface. This perfectly relaxed

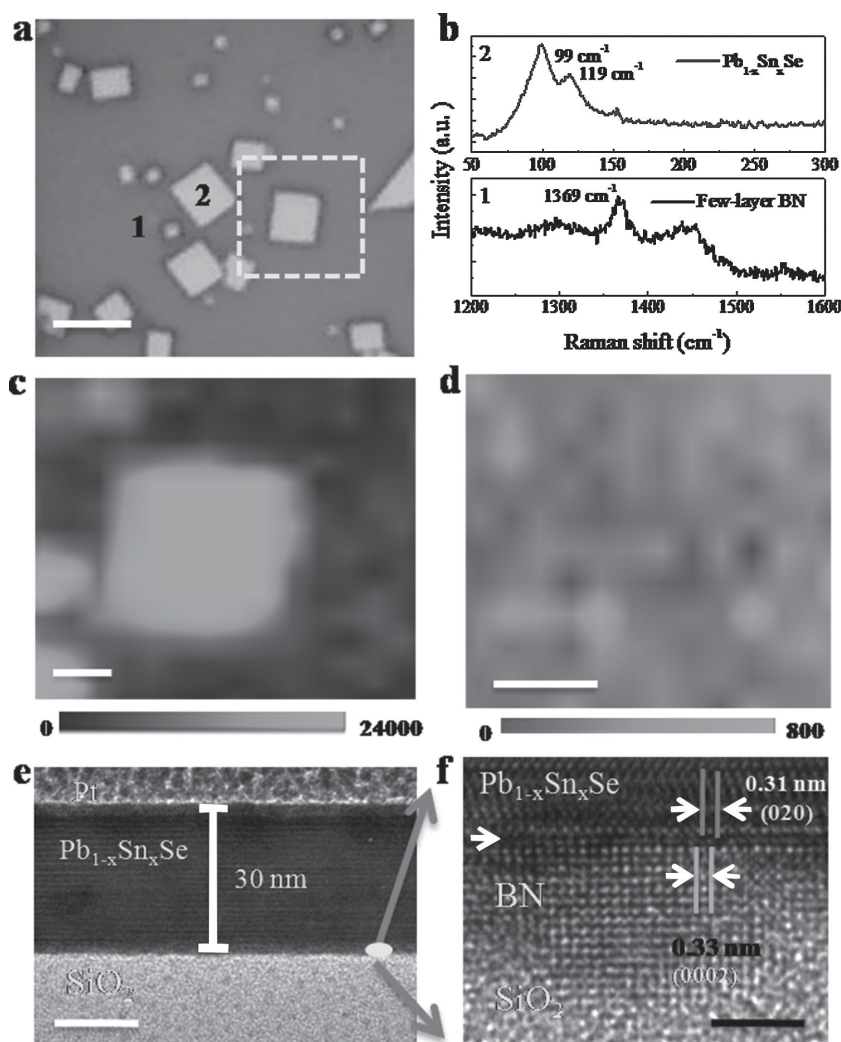


**Figure 2.** Characterization of few-layer BN/Pb<sub>1-x</sub>Sn<sub>x</sub>Se nanoplate heterostructure. a) Optical image of Pb<sub>1-x</sub>Sn<sub>x</sub>Se nanoplates on few-layer BN/SiO<sub>2</sub> substrate. Scale bar = 5 μm. b) Raman spectra obtained from locations 1 and 2 in (a). c, d) are Raman intensity mappings of Pb<sub>1-x</sub>Sn<sub>x</sub>Se nanoplate at 99 cm<sup>-1</sup> and *h*-BN at 1369 cm<sup>-1</sup>, respectively. Scale bars in (c) and (d) are 2 and 4 μm, respectively. The Raman intensity mappings are got from the region signed by yellow and dashed square in (a). e) Cross-section TEM of SiO<sub>2</sub>/few-layer BN/Pb<sub>1-x</sub>Sn<sub>x</sub>Se nanoplate heterostructure. A layer of Pt thin film was deposited on the sample to prevent the Pb<sub>1-x</sub>Sn<sub>x</sub>Se nanoplate from contamination during the ion milling process. Scale bar = 15 nm. f) High-resolution TEM of few-layer BN/Pb<sub>1-x</sub>Sn<sub>x</sub>Se nanoplate heterostructure which denotes a clear interface between BN and Pb<sub>1-x</sub>Sn<sub>x</sub>Se. The red arrow shows the interface. The lattice mismatch between (020) surface of Pb<sub>1-x</sub>Sn<sub>x</sub>Se and (0002) surface of BN reaches 6.1%. Scale bar = 3 nm.

heterostructure is expected to have prominent electronic and optoelectronic properties due to its long-range order in the interface with minimal density of defects states. The high-resolution TEM (HRTEM) of single Pb<sub>1-x</sub>Sn<sub>x</sub>Se nanoplate is shown in Figure S5 (Supporting Information); the sample shows distinct lattice fringes and well-defined selected area electron diffraction (SAED) pattern, indicating the Pb<sub>1-x</sub>Sn<sub>x</sub>Se nanoplate is highly single-crystalline. The growth dynamics of Pb<sub>1-x</sub>Sn<sub>x</sub>Se nanoplate has been well illuminated in our previous work.<sup>[19]</sup> Here few-layer BN replaces the role of mica as the vdW substrate which (1) allows the growth of defect-free overlayer with different crystalline symmetry to that of substrate, and (2) facilitates the migration of adatoms

on the surface of few-layer BN and thus accelerates the growth of Pb<sub>1-x</sub>Sn<sub>x</sub>Se nanoplate along lateral direction.

Above results indicate that few-layer BN serves as a buffer layer which allows the growth of Pb<sub>1-x</sub>Sn<sub>x</sub>Se nanoplates on SiO<sub>2</sub>/Si without the requirements of lattice matching. What's interesting here is that the growth of Pb<sub>1-x</sub>Sn<sub>x</sub>Se nanoplate selectively takes place on those area which are covered by few-layer BN under certain optimized growth condition. The crystals growth proceeds with the nucleation at certain disordered sites which are highly chemically active. The growth of Pb<sub>1-x</sub>Sn<sub>x</sub>Se nanoplate on few-layer BN likely initiates from edges with high density of defect states. However, Pb<sub>1-x</sub>Sn<sub>x</sub>Se nanoplates should have grown on SiO<sub>2</sub>/Si since surface of highly disordered SiO<sub>2</sub> also possesses large amount of trap centers. Since the interface between Pb<sub>1-x</sub>Sn<sub>x</sub>Se nanoplates and few-layer BN is highly ordering without apparent lattice distortion, we conclude the growth of Pb<sub>1-x</sub>Sn<sub>x</sub>Se nanoplates after nucleation is dominated by vdW interaction. Nevertheless, surface of SiO<sub>2</sub>/Si is filled with unpaired electrons which will interact with adatoms through strong chemical bonding. Hence it is reasonable to infer this chemical reaction has not been activated at given experimental conditions. This novel behavior enables us to construct Pb<sub>1-x</sub>Sn<sub>x</sub>Se nanoplates-based devices array by preparing regular few-layer BN pattern.

Direct growth of Pb<sub>1-x</sub>Sn<sub>x</sub>Se nanoplates on SiO<sub>2</sub>/Si enables in situ fabrication of field effect transistors (FET) by standard electron-beam lithography (see the Experimental Section for more information about the devices fabrication and measurement). **Figure 3a** shows the room-temperature transfer ( $I_{ds}-V_g$ ) characteristics of one representative FET, displaying *p*-type transistor behavior and small

but finite hysteresis, likely due to the ambient molecules tapped at the Pb<sub>1-x</sub>Sn<sub>x</sub>Se nanoplate/Au interface. Field effect mobility ( $\mu$ ) of these devices is estimated by the following equation

$$\mu = (\Delta I_{ds} / \Delta V_g) \times Ld / (WV_{ds}\epsilon_0\epsilon_r) \quad (1)$$

where  $L$  and  $W$  are the channel length and width, respectively,  $V_{ds}$  is the voltage bias,  $d$  is the thickness of SiO<sub>2</sub> (300 nm),  $\epsilon_0 = 8.844 \times 10^{-14}$  F cm<sup>-1</sup>, and  $\epsilon_r$  equals 3.9. The field effect mobility is in the range of 0.73–4.90 cm<sup>2</sup> V<sup>-1</sup> s<sup>-1</sup>, which is comparable to that of some layered materials<sup>[9,22]</sup>

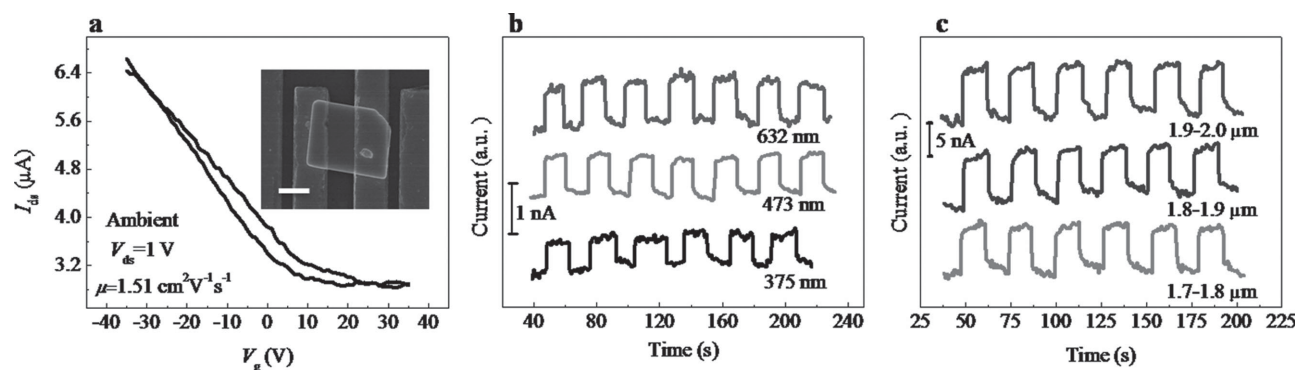


**Figure 3.** Field-induced transport and mid-infrared detection at room temperature. a) Transfer ( $I_{ds}$ – $V_g$ ) characteristics of one representative FET, displaying  $p$ -type transistor behavior with field effect mobility of  $1.51 \text{ cm}^2 \text{ V}^{-1} \text{ s}^{-1}$ . The inset shows the SEM image of corresponding device. Scale bar =  $1 \text{ }\mu\text{m}$ . b) Time-traced photoresponse at 375, 473, and 632 nm. c) Mid-infrared detection of  $\text{Pb}_{1-x}\text{Sn}_x\text{Se}$  nanoplates at  $1.7$ – $2.0 \text{ }\mu\text{m}$ . The photoresponsivity is estimated to be  $318 \text{ mA W}^{-1}$  at  $1.9$ – $2.0 \text{ }\mu\text{m}$ .

and molecule crystals.<sup>[12]</sup> The on/off ratio of  $\text{Pb}_{1-x}\text{Sn}_x\text{Se}$  nanoplates FET shown in Figure 3 is 2.2. The low on/off ratio could be understood by the fact that, as a narrow band-gap semiconductor, the carrier density is high due to the strong thermal excitation.

The temperature and composition dependence of “ $\text{Pb}_{1-x}\text{Sn}_x\text{Se}$  band gap”<sup>[23]</sup> is given by

$$E_g = 0.13 + (4.5 \times 10^{-4} \text{ deg}^{-1})T - 0.89x \quad (2)$$

where  $T$  means temperature and  $x$  denotes Sn content. Therefore band gaps of  $\text{Pb}_{0.4}\text{Sn}_{0.6}\text{Se}$  at 300, 180, 140, 120, 100, and 80 K are  $-0.27$ ,  $-0.32$ ,  $-0.34$ ,  $-0.35$ ,  $-0.36$ , and  $-0.37 \text{ eV}$ , respectively. All the values are minus since conduction band exchanges with valence band when the Sn content exceeds 0.38. The narrow band gap endows  $\text{Pb}_{1-x}\text{Sn}_x\text{Se}$  nanoplates with important applications in infrared detection. As revealed by Figure 3b,c, the two-terminal  $\text{Pb}_{1-x}\text{Sn}_x\text{Se}$  device (Figure S6, Supporting Information) exhibits remarkable photoresponse with ultrabroad detection spectra from UV to mid-infrared at ambient temperature. Here light intensity ( $P$ ) of 375, 473, 632 nm, and each infrared waveband ( $1.7$ – $1.8$ ,  $1.8$ – $1.9$ , and  $1.9$ – $2.0 \text{ }\mu\text{m}$ ) was set to  $302.9$ ,  $232$ ,  $82.6$ , and  $226.5 \text{ mW cm}^{-2}$ , respectively. As clarified by time-resolved photoresponse in Figure 3b,c, the device shows highly stability at various wavelength, which exhibits almost the same level of photocurrent ( $I_{ph}$ ) and dark current ( $I_{dark}$ ) with light on and off. The photoresponsivity ( $R$ ), defined as  $I_{ph}/P$ , is estimated to be  $318 \text{ mA W}^{-1}$  for detection at mid-infrared waveband  $1.9$ – $2.0 \text{ }\mu\text{m}$ . Here,  $I_{ph}$  represents the differences between  $I_{on}$  and  $I_{dark}$  and  $2 \text{ V}$  voltage bias is applied. More details regarding the measurements of photoresponse can be acquired from the Supporting Information. It is worth emphasizing here high-efficient response of  $\text{Pb}_{1-x}\text{Sn}_x\text{Se}$  nanoplates to long wavelength of  $1.7$ – $2.0 \text{ }\mu\text{m}$ , which lies in one of the infrared atmospheric windows ( $1.5$ – $1.9 \text{ }\mu\text{m}$ ), suggesting their huge application potential<sup>[24]</sup> in military communication, environmental monitoring, remote sensing, fiber-optic communications, night-time surveillance, emerging medical imaging modalities, etc. We believe that due to its narrow band gap ( $\approx 0.4 \text{ eV}$ ) and high crystal quality grown on BN, the

efficient detection of  $\text{Pb}_{1-x}\text{Sn}_x\text{Se}$  2D nanoplates can be extended to  $3$ – $5 \text{ }\mu\text{m}$ , another important atmosphere window.

To deeply understand the performance of  $\text{Pb}_{1-x}\text{Sn}_x\text{Se}$  nanoplates-based photodetectors, we further investigated the temperature effect on the photoresponse. Here, unless specifically noted, all measurements are implemented under high vacuum of  $4 \times 10^{-4} \text{ mbar}$  with the voltage bias of  $2 \text{ V}$ . Figure 4a represents the time-dependent  $I_{ph}$  at various temperature under irradiation of 632 nm laser ( $82.6 \text{ mW cm}^{-2}$ ). The current curves tend to be smoother with the temperature decreasing from 300 to 80 K, which is likely because of weaker electron–phonon scattering at low temperature. Light intensity dependence of photocurrent at 473 nm laser is further executed as shown in Figure 4b. The device shows apparent photoresponse even when the light intensity drops to  $0.1 \text{ mW cm}^{-2}$ , confirming the high detection sensitivity of our device. Next we will discuss more about temperature effect on the photoresponse of 632 nm laser, which presents interesting optoelectronic behavior. The response time ( $\tau_{rising}$ ) and recovery time ( $\tau_{decay}$ ), distributing between 0.8 and 1.6 s, hardly changes within the range of uncertainty when the temperature decreases from 300 to 80 K even when the experiments were performed at ambient temperature. From this observation, we can infer photoresponse of  $\text{Pb}_{1-x}\text{Sn}_x\text{Se}$  nanoplate has not been affected by trapping centers of atmospheric molecules and thermally activated defects, both of which will deteriorate the optoelectronic performance through capturing photogenerated carriers.<sup>[25]</sup> One possible explanation is that surface of  $\text{Pb}_{1-x}\text{Sn}_x\text{Se}$  nanoplate is chemically inactive, and both the interface and body are highly ordering with low density of defects.

To get better insight into how temperature influences the photoresponse of  $\text{Pb}_{1-x}\text{Sn}_x\text{Se}$  nanoplate,  $I_{dark}$  and on/off ratio ( $I_{on}/I_{dark}$ ) are extracted from the raw data as shown in Figure 4d. And  $I_{on}$ ,  $I_{dark}$ , and  $I_{ph}$  are plotted together in Figure 4e for comparison. On/off ratio continuously increases from 1.0 to 82.5 with the decrease of temperature from 300 to 80 K (Figure 4d). In addition, the detectivity ( $D$ ), representing the ability to detect signal from noise, apparently increases from  $1.14 \times 10^{12}$  at 300 K to  $7.72 \times 10^{13}$  at 80 K (Figure 4f). Here  $D$  is given by

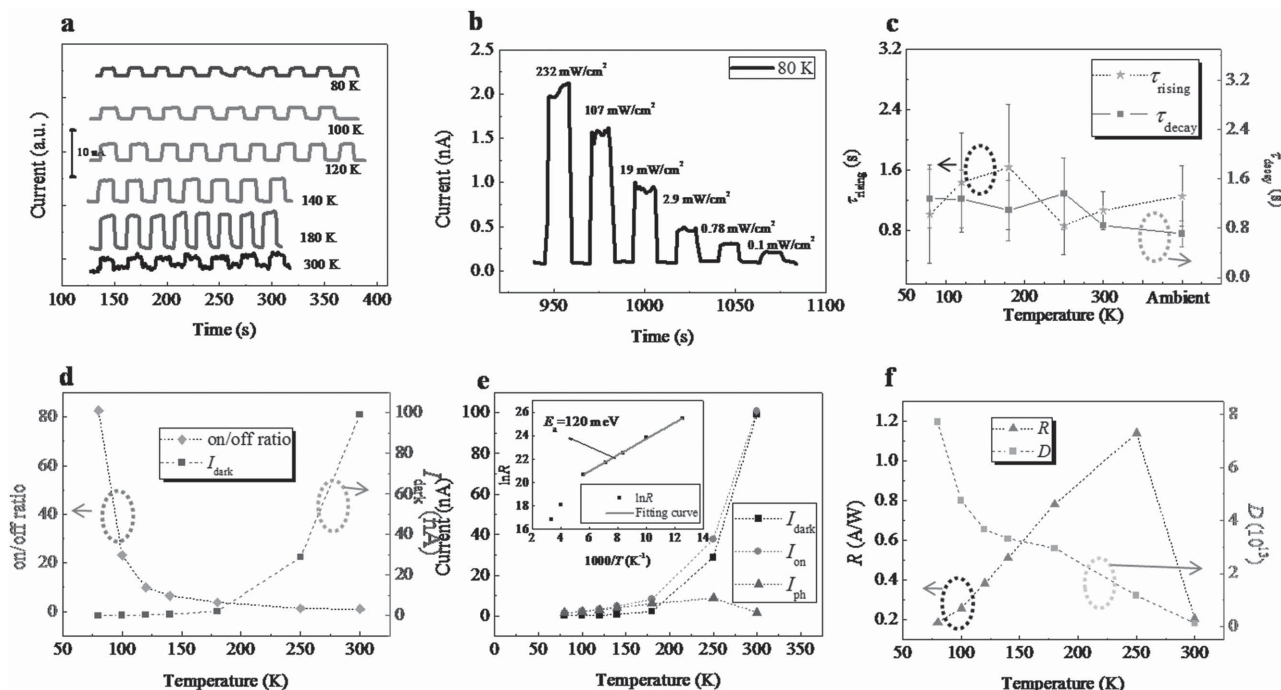


**Figure 4.** Temperature dependence of photoresponse. a) Time-traced photoresponse at various temperatures under illumination of 632 nm laser. b) Light intensity-dependent photoresponse at 80 K with irradiation of 473 nm laser. Comparison of c) response time ( $\tau_{\text{rising}}$ ) and decay time ( $\tau_{\text{decay}}$ ), d) on/off ratio and  $I_{\text{dark}}$ , e)  $I_{\text{dark}}$ ,  $I_{\text{on}}$ , and  $I_{\text{ph}}$ , and f) photoresponsivity and detectivity at various temperatures. The photoresponsivity sharply increases from  $0.21 \text{ A W}^{-1}$  at 300 K to  $1.14 \text{ A W}^{-1}$  at 250 K and then drops to  $0.19 \text{ A W}^{-1}$  at 80 K, which is possibly caused by increasing height of Schottky barrier between Cr/Au electrode and  $\text{Pb}_{1-x}\text{Sn}_x\text{Se}$  nanoplate with the decrease of temperature. However, the detectivity obviously increases from  $1.14 \times 10^{12}$  at 300 K to  $7.72 \times 10^{13}$  at 80 K. Comprehensively considering photoelectric efficiency, detectivity, and response speed, 150–250 K is suggested to be the optimum work condition.

$$I_{\text{ph}}/P\sqrt{2qI_{\text{dark}}} \quad (3)$$

where  $q$  is the unit electron charge. Both increase of on/off ratio and  $D$  would be explained by that the dark current is notably suppressed at low temperature. However, the photocurrent and photoresponsivity do not monotonously enhance with increase of on/off ratio.  $I_{\text{ph}}$  firstly increases from 1.58 nA at 300 K to a maxima of 8.77 nA at 250 K (Figure 4e). And then  $I_{\text{ph}}$  gradually decreases to 1.42 nA at 80 K. Correspondingly, as shown in Figure 4f,  $R$  sharply increases from  $0.21 \text{ A W}^{-1}$  at 300 K to  $1.14 \text{ A W}^{-1}$  at 250 K and then drops to  $0.19 \text{ A W}^{-1}$  at 80 K. For elucidating this novel behavior, one needs to take into account Schottky barrier. At high temperature, the energy scale of temperature ( $kT$ ) is enough high to overcome the Schottky barrier ( $\Phi$ ).<sup>[26]</sup> Hence the thermal-excited and photogenerated electrons are fully activated to participate charge transport. That is the reason we see the current ( $I$ )–voltage ( $V$ ) curve at 300 K is nearly linear at 300 K (Figure S7, Supporting Information). However, although the device exhibits Ohmic contact at this temperature, its photoresponsivity is relatively low ( $0.21 \text{ A W}^{-1}$ ), likely because overmuch thermal-excited carriers overwhelm the transport contribution of photogenerated electron–hole pairs. As shown in the inset of Figure 4e, thermal activated energy estimated from the linear region of  $\ln R$  versus  $1/T$  at low temperature is about 120 meV.  $\ln R$  abruptly decreases when temperature reaches 250 K since the localized charges have been fully excited at high temperature. The  $I$ – $V$  curve

at 250 K is more dissymmetry compared with that at 300 K (Figure S7, Supporting Information). In this case, the dark current dramatically decreases because (1) the numbers of thermal-excited carriers reduce, and (2) thermionic emission over the Schottky barrier also weakens. However, the numbers of photoexcited electrons hardly change as the irradiation intensity and area remain constant during the whole experiment process. Hence, the total photocurrent sharply increases due to suppression of dark current. When the temperature further decreases from 250 to 80 K, the efficient photocurrent considerably diminishes because of sharply decreased thermionic emission at low temperature. The same phenomenon has also occurred in another device as shown in Figure S8 (Supporting Information). Above results demonstrate the Schottky barrier plays a dominant role in modulating the transport of both thermal-motivated and photogenerated carriers at low temperature. If we comprehensively consider photoelectric efficiency, detectivity, and response speed, 150–250 K should be the optimum work conditions.

This work demonstrates a surface engineering with layered materials as the buffer layer for designing a controllable synthesis of  $\text{Pb}_{1-x}\text{Sn}_x\text{Se}$  nanoplates on  $\text{SiO}_2/\text{Si}$  substrates, which features highly compatibility with current Si-based integration circuit industry. Furthermore, special 2D geometry of  $\text{Pb}_{1-x}\text{Sn}_x\text{Se}$  nanoplate makes the gate voltage modulation more efficient compared with 1D or bulk architecture due to its ultrathin thickness in the vertical direction. And

compared with traditional HgCdTe or quantum well infrared photodetector which are prepared by complicated and expensive molecular beam epitaxy or metalorganic chemical vapor deposition, the proposed mid-infrared detector based on few-layer BN/Pb<sub>1-x</sub>Sn<sub>x</sub>Se nanoplate heterostructure is much more cost-efficient and simple fabrication process, suggesting its promising applications in military communication, environmental monitoring, remote sensing, fiber-optic communications, night-time surveillance, and emerging medical imaging modalities. We believe that the concept developed in this work can be generalized to build other integrated systems with architecture of SiO<sub>2</sub>/2D layered materials/2D nonlayered semiconductors for novel and practical electronic and optoelectronic devices by combining the unique advantages of constitute elements. One thing needs to be mentioned that, although our device exhibits high room-temperature carrier mobility, the on/off ratio of back-gated FET is low at room temperature. This is likely because of sufficient thermal excitation due to narrow band gap of Pb<sub>1-x</sub>Sn<sub>x</sub>Se. However, PbSe nanowires have demonstrated high on/off ratio ( $\approx 10^6$ ) at room temperature by surface functionalization.<sup>[27]</sup> Therefore, we could conduct further surface or interface engineering to improve the on/off ratio as well as mobility of Pb<sub>1-x</sub>Sn<sub>x</sub>Se nanoplates-based electronic and optoelectronic devices.

In summary, we have performed a vdWE growth of Pb<sub>1-x</sub>Sn<sub>x</sub>Se nanoplates with thickness ranging from 10 to 70 nm on amorphous SiO<sub>2</sub>/Si substrates through introducing a buffer layer of few-layer BN. Pb<sub>1-x</sub>Sn<sub>x</sub>Se nanoplates are found to selectively grow on the areas which are covered by few-layer BN with a well-identified interface between Pb<sub>1-x</sub>Sn<sub>x</sub>Se nanoplates and few-layer BN, showing the growth of Pb<sub>1-x</sub>Sn<sub>x</sub>Se nanoplates is dominated by vdW interaction. Benefiting from the highly compatible of SiO<sub>2</sub>/Si substrate with the existing Si-based semiconductor industry, FETs based on Pb<sub>1-x</sub>Sn<sub>x</sub>Se nanoplates are in situ fabricated on SiO<sub>2</sub>/Si. The devices exhibit room-temperature field effect mobility of  $\approx 0.73\text{--}4.90\text{ cm}^2\text{ V}^{-1}\text{ s}^{-1}$  that is comparable with some layered materials and molecular crystals. Furthermore, Pb<sub>1-x</sub>Sn<sub>x</sub>Se nanoplates show high-efficient room-temperature photoresponse with detection wavelength extending to 1.9–2.0  $\mu\text{m}$  which matches with one of the infrared atmospheric windows (1.5–1.9  $\mu\text{m}$ ), suggesting the great applications potential of Pb<sub>1-x</sub>Sn<sub>x</sub>Se nanoplates in military communication, environmental monitoring, and remote sensing. The proposed scheme provides a clear path toward designing epitaxial growth of high-quality crystals on functional substrates for future high-performance and Si-compatible electronic and optoelectronic devices.

## Experimental Section

**Synthesis and Transfer of Few-Layer BN:** Copper foil (99.98%, 25  $\mu\text{m}$  thick) was used as a metal catalyst substrate. After copper foil was washed with acetic acid and electropolished, it was placed in a temperature zone at the tube furnace. Then, the copper foil was annealed at 1050  $^\circ\text{C}$  with the protection of H<sub>2</sub> (15 sccm) for

40 min to remove possible residual substances and to obtain a smooth surface. Growth was initiated by heating the ammonia borane (NH<sub>3</sub>-BH<sub>3</sub>) (97% purity, Sigma-Aldrich) to 100  $^\circ\text{C}$  and maintained for 5 min. After growth, the tube furnace was cooled down to room temperature. *h*-BN/Cu was spin-coated with polymethyl methacrylate (PMMA) at 3000 rpm for 1 min. Then, PMMA/*h*-BN/Cu was immersed in an aqueous solution of 0.1 M NaOH using as a cathode, Au was used as an anode. PMMA/*h*-BN was completely detached from the copper foil at 10 V under constant flow within 1 min. Deionized water rinsed PMMA/*h*-BN several times. PMMA/*h*-BN was transferred onto SiO<sub>2</sub>/Si or polyimide substrate and dried at 50  $^\circ\text{C}$  for 3 min. Finally, PMMA was completely removed with dichloromethane at 50  $^\circ\text{C}$ .

**Chemical Vapor Deposition of Pb<sub>1-x</sub>Sn<sub>x</sub>Se Nanoplates:** We used horizontal vacuum tube furnace with single temperature zone to synthesize Pb<sub>1-x</sub>Sn<sub>x</sub>Se nanoplates. 0.2 g Pb and 0.2 g SnSe powder (99.99 %, Alfa Aesar) were mixed, ground, and then placed in the center of quartz tube. Few-layer BN covered SiO<sub>2</sub>/Si substrates were put in the downstream area. The pump was firstly applied to vacuum the quartz tube. And then Ar gas was used to flush the quartz tube several times. Ar gas was fed with a constant flow rate 20 sccm by maintaining tube pressure of 69 Pa during the growth process. The source and substrate temperatures were set to 600 and 460  $^\circ\text{C}$ , respectively. The duration of the reaction process was maintained for 1 min. After that the furnace was allowed to cool naturally down to room temperature.

**Characterization:** Field emission scanning electron microscopy (FESEM) S4800 (Tokyo, Japan) and AFM (Veeco Multimode) were used to characterize the morphologies of few-layer BN and Pb<sub>1-x</sub>Sn<sub>x</sub>Se nanoplates. Electron EDX spectroscopy attached to the FESEM was applied to characterize the composition. Crystal microstructures were acquired by TEM, HRTEM, and SAED on FEI Tecnai F20. The crystal quality of Pb<sub>1-x</sub>Sn<sub>x</sub>Se nanoplates was further characterized by Raman (Renishaw InVia, 532 nm excitation laser). The samples for cross-section TEM of few-layer BN/Pb<sub>1-x</sub>Sn<sub>x</sub>Se nanoplate heterostructure were prepared by focused ion beam. In order to protect the sample during the ion milling process, Au and Pt layer was firstly deposited on the sample.

**Device Fabrication and Measurements:** The electrical contact patterns were fabricated by standard electron-beam lithography. Then 10 nm Cr and 150 nm Au were deposited on samples by thermal evaporation. The field-induced transport and photoresponse were performed in a manual probe station (Everbeing, BD4) equipped with a Keithley 4200 semiconductor characterization system. 375, 473, and 632 nm lasers were employed to irradiate the samples. For the infrared detection, the White Laser (SC400-2) equipped with high-power supercontinuum was used to simultaneously output eight monochromatic light with width of 2–3 nm each time. The average spectra power intensity is about 1 mW nm<sup>-1</sup>.

## Supporting Information

Supporting Information is available from the Wiley Online Library or from the author.

## Acknowledgements

Q.W. and Y.W. contributed equally to this work. This work at National Center for Nanoscience and Technology was supported by 973 Program of the Ministry of Science and Technology of China (No. 2012CB934103), the 100-Talents Program of the Chinese Academy of Sciences (No. Y1172911ZX), the National Natural Science Foundation of China (Nos. 21373065 and 61474033), and Beijing Natural Science Foundation (No. 2144059).

- [1] a) Y. Hao, M. Bharathi, L. Wang, Y. Liu, H. Chen, S. Nie, X. Wang, H. Chou, C. Tan, B. Fallahzad, *Science* **2013**, *342*, 720; b) J. Kim, C. Bayram, H. Park, C.-W. Cheng, C. Dimitrakopoulos, J. A. Ott, K. B. Reuter, S. W. Bedell, D. K. Sadana, *Nat. Commun.* **2014**, *5*, 4836.
- [2] a) M. H. Huang, S. Mao, H. Feick, H. Yan, Y. Wu, H. Kind, E. Weber, R. Russo, P. Yang, *Science* **2001**, *292*, 1897; b) H. Li, J. Cao, W. Zheng, Y. Chen, D. Wu, W. Dang, K. Wang, H. Peng, Z. Liu, *J. Am. Chem. Soc.* **2012**, *134*, 6132.
- [3] C. Dean, A. Young, I. Meric, C. Lee, L. Wang, S. Sorgenfrei, K. Watanabe, T. Taniguchi, P. Kim, K. Shepard, *Nat. Nanotechnol.* **2010**, *5*, 722.
- [4] E. Hwang, S. Adam, S. D. Sarma, *Phys. Rev. Lett.* **2007**, *98*, 186806.
- [5] a) I. Hulea, S. Fratini, H. Xie, C. Mulder, N. Iossad, G. Rastelli, S. Ciuchi, A. Morpurgo, *Nat. Mater.* **2006**, *5*, 982; b) M. Calhoun, C. Hsieh, V. Podzorov, *Phys. Rev. Lett.* **2007**, *98*, 096402; c) W. Feng, W. Zheng, W. Cao, P. Hu, *Adv. Mater.* **2014**, *26*, 6587; d) X. Wang, J. B. Xu, C. Wang, J. Du, W. Xie, *Adv. Mater.* **2011**, *23*, 2464.
- [6] C. H. Lee, D. R. Kim, X. Zheng, *P. Natl. Acad. Sci. USA* **2010**, *107*, 9950.
- [7] H. Li, J. Wu, X. Huang, Z. Yin, J. Liu, H. Zhang, *ACS Nano* **2014**, *8*, 6563.
- [8] K. S. Novoselov, A. K. Geim, S. Morozov, D. Jiang, Y. Zhang, S. Dubonos, I. Grigorieva, A. Firsov, *Science* **2004**, *306*, 666.
- [9] S. Najmaei, Z. Liu, W. Zhou, X. Zou, G. Shi, S. Lei, B. I. Yakobson, J.-C. Idrobo, P. M. Ajayan, J. Lou, *Nat. Mater.* **2013**, *12*, 754.
- [10] a) Y. Guo, M. Aisijiang, K. Zhang, W. Jiang, Y. Chen, W. Zheng, Z. Song, J. Cao, Z. Liu, H. Peng, *Adv. Mater.* **2013**, *25*, 5959; b) M. Lin, D. Wu, Y. Zhou, W. Huang, W. Jiang, W. Zheng, S. Zhao, C. Jin, Y. Guo, H. Peng, *J. Am. Chem. Soc.* **2013**, *135*, 13274.
- [11] a) M. I. B. Utama, F. J. Belarre, C. Magen, B. Peng, J. Arbiol, Q. Xiong, *Nano Lett.* **2012**, *12*, 2146; b) M. I. B. Utama, Q. Zhang, J. Zhang, Y. Yuan, F. J. Belarre, J. Arbiol, Q. Xiong, *Nanoscale* **2013**, *5*, 3570; c) A. Koma, *Thin Solid Films* **1992**, *216*, 72.
- [12] a) C. H. Lee, T. Schiros, E. J. Santos, B. Kim, K. G. Yager, S. J. Kang, S. Lee, J. Yu, K. Watanabe, T. Taniguchi, *Adv. Mater.* **2014**, *26*, 2812; b) D. He, Y. Zhang, Q. Wu, R. Xu, H. Nan, J. Liu, J. Yao, Z. Wang, S. Yuan, Y. Li, *Nat. Commun.* **2014**, *5*, 5162.
- [13] a) L. Britnell, R. Gorbachev, R. Jalil, B. Belle, F. Schedin, A. Mishchenko, T. Georgiou, M. Katsnelson, L. Eaves, S. Morozov, *Science* **2012**, *335*, 947; b) R. De Boer, M. Gershenson, A. Morpurgo, V. Podzorov, *Phys. Status Solidi A* **2004**, *201*, 1302; c) R. De Boer, A. Morpurgo, *Phys. Rev. B* **2005**, *72*, 073207.
- [14] K. K. Kim, A. Hsu, X. Jia, S. M. Kim, Y. Shi, M. Hofmann, D. Nezich, J. F. Rodriguez-Nieva, M. Dresselhaus, T. Palacios, *Nano Lett.* **2011**, *12*, 161.
- [15] G. Lu, T. Wu, Q. Yuan, H. Wang, H. Wang, F. Ding, X. Xie, M. Jiang, *Nat. Commun.* **2015**, *6*, 6160.
- [16] a) P. Dziawa, B. Kowalski, K. Dybko, R. Buczko, A. Szczerbakow, M. Szot, E. Łusakowska, T. Balasubramanian, B. M. Wojek, M. Berntsen, *Nat. Mater.* **2012**, *11*, 1023; b) J. Dixon, G. Hoff, *Phys. Rev. B* **1971**, *3*, 4299.
- [17] a) T. H. Hsieh, H. Lin, J. Liu, W. Duan, A. Bansil, L. Fu, *Nat. Commun.* **2012**, *3*, 982; b) L. Fu, *Phys. Rev. Lett.* **2011**, *106*, 106802.
- [18] a) Q. Wang, M. Safdar, K. Xu, M. Mirza, Z. Wang, J. He, *ACS Nano* **2014**, *8*, 7497; b) P. K. Mohseni, A. Behnam, J. D. Wood, X. Zhao, K. J. Yu, N. C. Wang, A. Rockett, J. A. Rogers, J. W. Lyding, E. Pop, *Adv. Mater.* **2014**, *26*, 3755; c) Y. Alaskar, S. Arafin, D. Wickramaratne, M. A. Zurbuchen, L. He, J. McKay, Q. Lin, M. S. Goorsky, R. K. Lake, K. L. Wang, *Adv. Funct. Mater.* **2014**, *24*, 6629.
- [19] Q. Wang, K. Xu, Z. Wang, F. Wang, Y. Huang, M. Safdar, X. Zhan, F. Wang, Z. Cheng, J. He, *Nano Lett.* **2015**, *15*, 1183.
- [20] Y. Shi, C. Hamsen, X. Jia, K. K. Kim, A. Reina, M. Hofmann, A. L. Hsu, K. Zhang, H. Li, Z.-Y. Juang, *Nano Lett.* **2010**, *10*, 4134.
- [21] a) S. Ovsyannikov, Y. Ponomov, V. Shchennikov, V. Mogilenskikh, *Phys. Status Solidi C* **2004**, *1*, 3110; b) Y. Ai-Ling, W. Hui-Zhen, L. Zhi-Feng, Q. Dong-Jiang, C. Yong, L. Jian-Feng, P. McCann, X. Fang, *Chin. Phys. Lett.* **2000**, *17*, 606.
- [22] Y. H. Lee, X. Q. Zhang, W. Zhang, M. T. Chang, C. T. Lin, K. D. Chang, Y. C. Yu, J. T. W. Wang, C. S. Chang, L. J. Li, *Adv. Mater.* **2012**, *24*, 2320.
- [23] M. M. Ali, S. M. Meshari, *J. Basrah Res.* **2011**, *37*, 50.
- [24] a) Y. Zhang, T. Liu, B. Meng, X. Li, G. Liang, X. Hu, Q. J. Wang, *Nat. Commun.* **2013**, *4*, 1811; b) Z. Sun, Z. Liu, J. Li, G. a. Tai, S. P. Lau, F. Yan, *Adv. Mater.* **2012**, *24*, 5878.
- [25] Z. Wang, K. Xu, Y. Li, X. Zhan, M. Safdar, Q. Wang, F. Wang, J. He, *ACS Nano* **2014**, *8*, 4859.
- [26] D. A. Neamen, *Semiconductor Physics and Devices: Basic Principles*, 3rd ed., McGraw-Hill New York **2003**.
- [27] a) R. Graham, D. Yu, *Nano Lett.* **2012**, *12*, 4360; b) D. K. Kim, T. R. Vemulkar, S. J. Oh, W.-K. Koh, C. B. Murray, C. R. Kagan, *ACS Nano* **2011**, *5*, 3230.

Received: July 09, 2015  
 Revised: July 13, 2015  
 Published online: August 25, 2015